

Cite this: *Chem. Sci.*, 2026, 17, 9168 All publication charges for this article have been paid for by the Royal Society of Chemistry

# Selenol-containing two-dimensional perovskite promotes visible-light-driven selective reduction of unsaturated ketones

Wenxuan Li,<sup>†a</sup> Lihao Liao,<sup>†a</sup> Guoying Yao,<sup>ab</sup> Jialong Liu,<sup>a</sup> Yilan Zhang,<sup>a</sup> Jingpeng Li,<sup>a</sup> Wangzhen Qiu,<sup>a</sup> Tao Zeng,<sup>†b</sup> Xiaodan Zhao<sup>†\*a</sup> and Zhenyu Yang<sup>†\*a</sup>

Semiconductors have shown growing promise for photocatalytic reactions due to their tunable band structures and efficient charge separation capabilities. Among them, metal halide perovskites (MHPs) have emerged as particularly attractive candidates owing to their intense light absorption and favorable charge transport properties; yet inefficient charge utilization often occurs in MHP-based photocatalysis due to undesired interfacial charge losses and lattice mismatches within the heterostructures. Herein, we report a two-dimensional perovskite (TMHP) photocatalyst, where selenol-functionalized organic cations are integrated into the lattice as both structural components and catalytic sites. This design enables efficient photoinduced charge separation and transfer from the [PbI<sub>4</sub>]<sup>2-</sup> layers to the selenol groups, achieving visible-light-driven reduction of  $\alpha,\beta$ -unsaturated ketones with up to 87% yield across diverse substrates. Mechanistic studies reveal a radical-mediated pathway facilitated by the polarized lattice environment. This work demonstrates a new strategy for engineering molecular functionality into semiconductor lattices and creating integrated, efficient photocatalytic systems.

Received 10th December 2025

Accepted 8th March 2026

DOI: 10.1039/d5sc09706a

rsc.li/chemical-science

## Introduction

Metal halide perovskites (MHPs) have emerged as a rapidly developing family of semiconductor materials due to their exceptional absorption coefficients, tunable band structures, and superior charge transport properties.<sup>1-3</sup> These features mostly originate from the unique characteristic band edge constructed by the hybridization between s-orbitals of the metal cations (*e.g.*, Pb<sup>2+</sup> and Sn<sup>2+</sup>) and p-orbitals of halide anions (*e.g.*, I<sup>-</sup>, Br<sup>-</sup>, and Cl<sup>-</sup>), which gives rise to direct bandgaps and favorable carrier dynamics.<sup>4-6</sup> Remarkably, MHPs have attracted considerable attention across diverse photocatalytic fields, including hydrogen production,<sup>7-9</sup> CO<sub>2</sub> reduction,<sup>10-13</sup> and organic synthesis such as C-H bond activation, C-X bond coupling (X = C, O, N, *etc.*),<sup>14-16</sup> and selective oxidation.<sup>17</sup> These examples demonstrate MHPs as multifunctional photocatalytic platforms where tailored electronic structures and dynamic interfaces enable efficient solar energy conversion beyond conventional semiconductors.<sup>18-20</sup>

The combination of MHPs with other materials through band alignment engineering has been widely explored to improve charge carrier separation. Existing strategies primarily involve solid-liquid interfacial transfer<sup>7,14,21</sup> or semiconductor heterostructures<sup>12,17,22-24</sup> (Fig. 1a). However, the multiphase approach often suffers from charge recombination and sluggish surface redox kinetics,<sup>16,25-27</sup> while heterostructures face challenges such as energy-level misalignment, interfacial degradation,<sup>28-31</sup> and the need for complex multi-step synthesis to achieve lattice matching.<sup>32-38</sup> A photocatalyst that intrinsically integrates light absorption, charge generation, and catalytic transformation within a single crystalline phase would be highly desirable to overcome these limitations.

Derived from conventional three-dimensional (3D) MHP structures by inserting bulky organic cations, two-dimensional MHPs (TMHPs) have shown unique features arising from the dimensionality reduction and structural modification induced by the spacers. The incorporation of organic cations with functional end groups leads to unrivalled tunability in the 2D lattice structures with programmable photophysical and chemical properties, which allows post-synthetic chemical reactions on TMHP scaffolds.<sup>1,5,39,40</sup> In addition, the atomically flat interface and sub-nanometer interlayer distance enable efficient energy and charge transfer between the inorganic layers and the organic cations, which is crucial for promoting the efficiency of TMHP-based energy conversion devices.<sup>41-43</sup> Earlier work employing TMHPs for catalytic reactions has

<sup>a</sup>MOE Laboratory of Bioinorganic and Synthetic Chemistry, Lehn Institute of Functional Materials, School of Chemistry, Sun Yat-sen University, Guangzhou, Guangdong, 510275, China. E-mail: zhaoxd3@mail.sysu.edu.cn; yangzhy63@mail.sysu.edu.cn

<sup>b</sup>Department of Chemistry, York University, Toronto, ON, M3J 1P3, Canada. E-mail: tzeng@yorku.ca

<sup>†</sup> These authors contributed equally to this work.



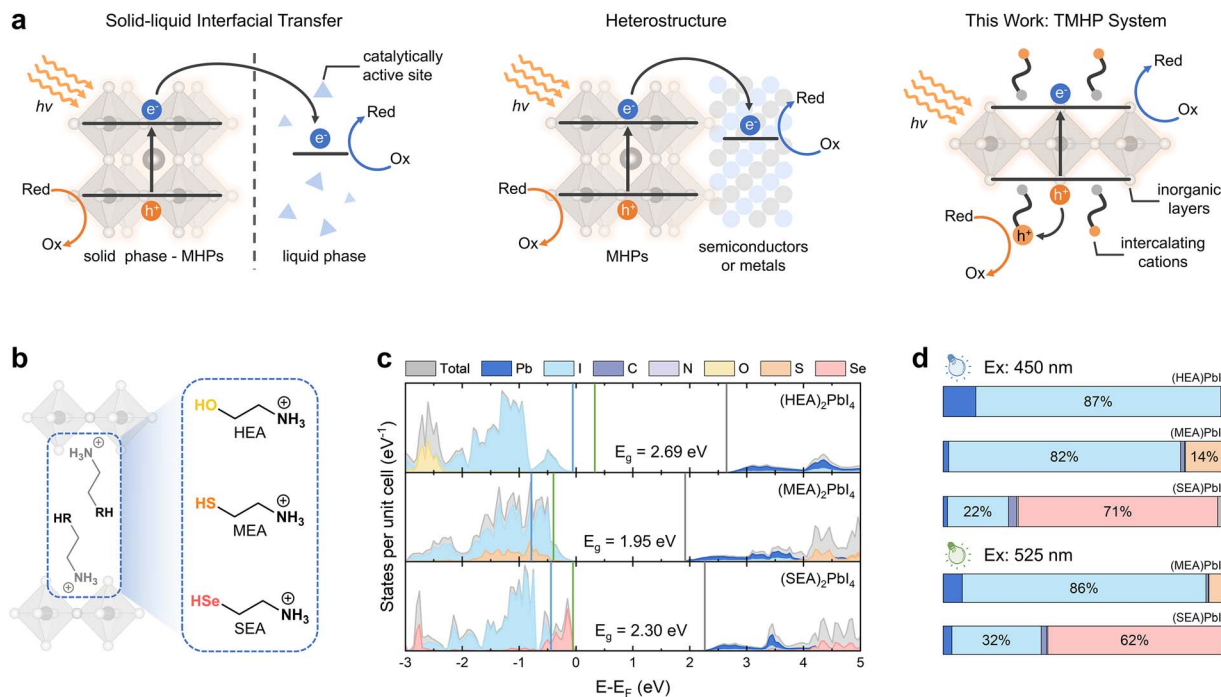


**Fig. 1** Rational design of the MHP-based photocatalyst. (a) Schematic diagram of charge transfer models in metal halide perovskites as photocatalysts: solid–liquid interfacial transfer, heterojunction, and the proposed TMHP system in this study. The TMHP system features a single-phase crystalline architecture in which light-absorbing inorganic layers are integrated with catalytically active organic cations. (b) General crystal structures of three types of TMHPs: (HEA)<sub>2</sub>PbI<sub>4</sub>, (MEA)<sub>2</sub>PbI<sub>4</sub>, and (SEA)<sub>2</sub>PbI<sub>4</sub> (HEA = NH<sub>3</sub><sup>+</sup>CH<sub>2</sub>CH<sub>2</sub>OH; MEA = NH<sub>3</sub><sup>+</sup>CH<sub>2</sub>CH<sub>2</sub>SH; SEA = NH<sub>3</sub><sup>+</sup>CH<sub>2</sub>CH<sub>2</sub>SeH), and (c) the corresponding DOS and pDOS patterns. All DOS/pDOS plots have been shifted so that the Fermi energy is at 0 eV for clear comparison of the near band edge states and band gap values. The valence band (VB) section sandwiched by blue and green lines represents the VB region where electrons can be excited by blue (450 nm) and green light (525 nm), respectively, to reach the conduction band minimum (shown with grey lines). (d) The contribution of pDOS in the valence band edges of the three types of TMHPs, in which electrons can be excited to the conduction band minimum under blue and green light irradiation, as defined in (c). The corresponding elemental proportion analyses are shown in Table S1. (HEA)<sub>2</sub>PbI<sub>4</sub> cannot be effectively excited by green light due to its relatively large bandgap (2.69 eV).

shown strong potential in photocatalytic applications. However, most of the TMHPs are only utilized as the light absorber, in which the photocatalytic efficiency still significantly relies on the efficient charge transfer to the external active sites.<sup>44–48</sup>

In this study, we sought to develop a new photocatalyst based on the rationally designed TMHP structures to integrate both the intense light-absorption and effective charge generation and transfer features of MHPs. The proposed TMHPs have suitable band gap (1.95–2.69 eV, Fig. 1c) to effectively convert visible light to charge carriers within the inorganic scaffolds,<sup>39,49</sup> which are effectively transferred to the functional end groups on the organic cations and directly used for the catalytic reactions (Fig. 1a). More importantly, the chalcogenol functional groups (–OH, –SH, and –SeH) have high chemical reactivity and have been widely used for organic reactions.<sup>50–56</sup> Therefore, we devised a TMHP structure containing a short organic chain with a unified formula of NH<sub>3</sub><sup>+</sup>–CH<sub>2</sub>–CH<sub>2</sub>–RH, where R=O, S, and Se (Fig. 1b). Density functional theory (DFT) calculations reveal that Se contributes 71% and 62% to the valence band edge within the excitation energy ranges of blue (450 nm) and green light (525 nm) irradiation, respectively, significantly exceeding the contributions of O and S atoms in analogues TMHP structures (Fig. 1c, d, S2 and Table S1). This dominance arises from several key factors: (i) diffuse 4p orbitals of the Se atom enhance

delocalization and orbital hybridization; (ii) its lower electronegativity (2.55 for Se vs. 3.44 for O and 2.58 for S) promotes greater electron density near the valence band edge; and (iii) the longer Se–H bond length and higher covalency strengthen orbital overlap compared to the more localized O/S counterparts. Collectively, these properties enhance Se atom's role in light absorption and charge carrier generation under visible excitation. These results suggest that selenol-containing TMHPs facilitate efficient photo-induced charge separation with excited electrons and holes migrating to the inorganic layer and the selenol active sites, respectively, thereby promoting redox reactions.

## Results and discussion

### Preparation of selenol-containing TMHP

To experimentally verify the functions of selenols in the MHP system, we prepared the selenol-containing TMHP (SEA)<sub>2</sub>PbI<sub>4</sub> (SEA = 2-hydroselenoethan-1-aminium (CCDC number: 2348172)) single crystals through a one-pot crystallization process (Fig. 2a). In an acidic aqueous solution, lead iodide (PbI<sub>2</sub>) and 2,2'-diselanediybis(ethan-1-aminium) (DSEA) cations were dissolved in hydrogen iodide (HI) solution (containing ≤1.5% of hypophosphorous acid (H<sub>3</sub>PO<sub>2</sub>)) to form the



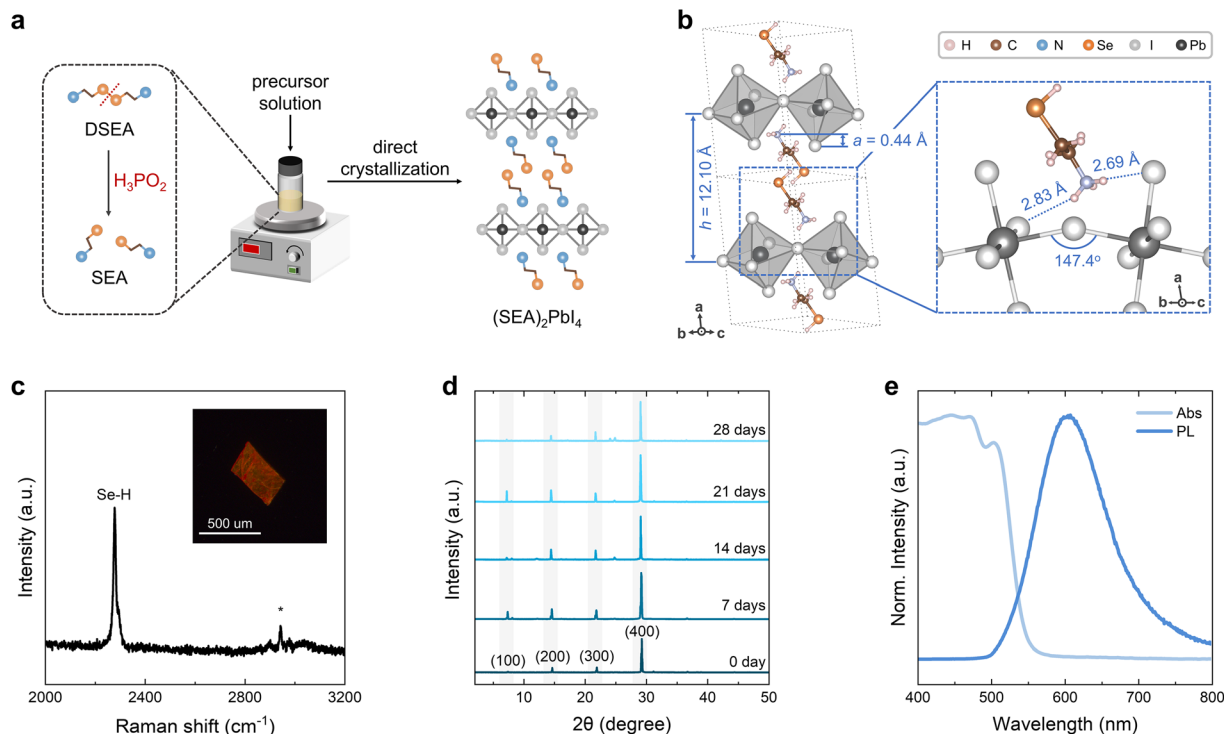


Fig. 2 Preparation and characterization of  $(\text{SEA})_2\text{PbI}_4$  crystals. (a) Schematic illustration of the preparation of  $(\text{SEA})_2\text{PbI}_4$ . (b) Single-crystal structure of  $(\text{SEA})_2\text{PbI}_4$ , where  $a$  and  $h$  refer to the penetration depth of the cations and the distance between two adjacent planes for the Pb centers in the  $[\text{PbI}_6]^{4-}$  octahedra, respectively. (c) Raman spectrum of the  $(\text{SEA})_2\text{PbI}_4$  crystals. An unknown impurity is denoted using an asterisk. Inset: stereo fluorescence microscope (SFM) image of a  $(\text{SEA})_2\text{PbI}_4$  crystal. (d) PXRD patterns of  $(\text{SEA})_2\text{PbI}_4$  crystals over time. (e) Absorption and PL spectra of  $(\text{SEA})_2\text{PbI}_4$ .

mother liquor. During this process, Se–Se bonds on DSEA cations are fully reduced by  $\text{H}_3\text{PO}_4$  to form SEA cations.<sup>56,57</sup> This transformation occurs simultaneously with the crystallization of the TMHP structure, yielding distinctive orange plate-like crystal structures. Detailed crystallographic information and the structural refinement data are available in Table S2.

### Analysis of structural and optical properties

Similar to OH- and SH-containing TMHPs,  $(\text{SEA})_2\text{PbI}_4$  has a layered structure with a corner-sharing  $[\text{PbI}_6]^{4-}$  octahedral network. However, due to the significantly longer Se–H bond length (Se–H: 1.29 Å vs. S–H: 1.19 Å, O–H: 0.84 Å) the spatial configuration of the SEA ligand differs greatly from the ‘curled’ structure of the HEA and MEA ligands, instead adopting an extended conformation aligned with the growth direction of the layered structure (Fig. S1). This leads to a significantly expanded interlayer spacing of 12.10 Å in  $(\text{SEA})_2\text{PbI}_4$ , which is 20% (2.05 Å) and 18% (1.81 Å) larger than those in  $(\text{HEA})_2\text{PbI}_4$  and  $(\text{MEA})_2\text{PbI}_4$ , respectively (Fig. S3). The H···I distances (2.69 Å and 2.84 Å) between the H atoms on ammonium end groups and the adjacent I atoms (Fig. 2b) in  $(\text{SEA})_2\text{PbI}_4$  are notably shorter than the summation of van der Waals radii of H and I atoms ( $\sim 3.1$  Å)<sup>58</sup> and those in  $(\text{HEA})_2\text{PbI}_4$  (2.75 Å) and  $(\text{MEA})_2\text{PbI}_4$  (2.86 to 2.92 Å), indicating strong hydrogen bonding interactions in  $(\text{SEA})_2\text{PbI}_4$  (Fig. S3). This interaction results in a positive penetration depth ( $a = 0.44$  Å) of intercalating cations, defined

as the distance between the primary  $\text{NH}_3^+$  group and the plane of terminal iodides, and also induces significant distortion of the inorganic framework, as evidenced by the small equatorial Pb–I–Pb angles of 147.6°, compared to those of  $(\text{HEA})_2\text{PbI}_4$  (159.8°),  $(\text{MEA})_2\text{PbI}_4$  (175.4°), and other reported TMHPs.<sup>59–61</sup>

We next investigated the stability of the selenol-containing TMHP structure. Due to the relatively low bond dissociation energy of Se–H (305 kJ mol<sup>-1</sup>) compared to S–H (344 kJ mol<sup>-1</sup>) and O–H (428 kJ mol<sup>-1</sup>), the selenol (Se–H) bond in free-standing molecules is much more prone to oxidation compared to thiols (S–H) and alcohols (O–H) and rapidly converts to diselenide (*i.e.*, –Se–Se–) groups even under mild oxidative conditions.<sup>56,62</sup> Surprisingly, Se–H bonds in  $(\text{SEA})_2\text{PbI}_4$  are relatively stable even under the exposure to air with humidity up to 80%, as the notable Se–H stretching vibration signal at 2277 cm<sup>-1</sup> persists (Fig. 2c).<sup>63,64</sup> The TMHP structure even remains unchanged after the storage under ambient conditions (20 °C, 60–80% of humidity) for 28 days (Fig. 2d and S4). We ascribe the enhanced stability of the Se–H bonds to the formation of compact TMHP structures in which Se–H bonds are closely packed within the layered structure and protected by the inorganic components (Fig. 2b).

To gain insights into the intrinsic properties of these TMHPs, we turned our attention to optical absorption and photoluminescence (PL) spectroscopy.  $(\text{SEA})_2\text{PbI}_4$  exhibits an absorption edge at 548 nm (Fig. 2e), corresponding to



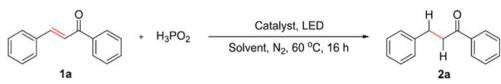
a bandgap of 2.20 eV as derived from Tauc plot analysis (Fig. S5). This experimental value is consistent with the DFT-calculated bandgap of 2.30 eV (Fig. 1c), with the slight discrepancy ( $\sim 0.1$  eV) attributable to DFT's typical underestimation of excitonic effects. The PL emission maximum at 608 nm (Stokes shift:  $\sim 60$  nm) further confirms a direct bandgap transition, consistent with the sharp absorption onset (Fig. 2e). Notably, the band gap of  $(\text{SEA})_2\text{PbI}_4$  is slightly larger than those of  $(\text{HEA})_2\text{PbI}_4$  (2.24 eV)<sup>49,65</sup> and  $(\text{MEA})_2\text{PbI}_4$  (2.09 eV),<sup>39</sup> reflecting the influence of the selenol group ( $-\text{SeH}$ ) on electronic structure modulation (Fig. 1c). The small Stokes shift and strong absorption in the blue-green region (450–550 nm) suggest low exciton binding energy and efficient light-harvesting capabilities, positioning  $(\text{SEA})_2\text{PbI}_4$  as a promising candidate for visible-light photocatalysis.

### Investigation on photocatalytic capability

Selenols are acidic and are readily deprotonated to form selenolate anions, which have been widely applied for nucleophilic addition/substitution.<sup>56,66–69</sup> However, because of Se–H bond's intrinsic instability against moisture and oxygen, most existing selenol-driven reactions heavily rely on the *in situ* formation of selenols (e.g., benzeneselenol,<sup>57,70</sup>  $\text{H}_2\text{Se}^{71,72}$  or metallic hydrogen selenide<sup>73</sup>), significantly limiting the applications of Se–H as a potential catalytically active site. Encouraged by the materials stability and the unique electronic structure, as well as the strong light absorption of  $(\text{SEA})_2\text{PbI}_4$ , we sought to investigate its potential as a MHP-based photocatalyst. In this composite catalyst, the lead halide component can effectively absorb photon energy and generate sufficient free charge carriers, which are transferred to the selenol component to facilitate redox reactions.

To verify the effectiveness of  $(\text{SEA})_2\text{PbI}_4$  as a photocatalyst, we selected  $\alpha,\beta$ -unsaturated carbonyl compounds as the substrates for demonstrating the capability of TMHPs for photoinduced selective redox reactions.<sup>74,75</sup> Specifically, chalcone was used as the model substrate due to its representative asymmetric enone model and well-defined redox behavior. The standard reaction was carried out under a nitrogen atmosphere and excited by visible-light irradiation with predesigned wavelengths, in which  $(\text{SEA})_2\text{PbI}_4$  and  $\text{H}_3\text{PO}_2$  were used as the photocatalyst and stoichiometric reductant, respectively. Among the commonly used solvents in selenol reduction, we selected hexane as the standard solvent, as the reaction with it showed the best performance among all tested solvents. This is likely due to its non-polar nature, which better preserves the structural integrity of the perovskite catalyst, affording the reduced product **2a** in a yield up to 81% (excitation wavelength  $\lambda_{\text{ex}} = 450$  nm, Table 1, entries 1–5, measured by  $^1\text{H}$  NMR using 1,3,5-trimethoxybenzene as the internal standard). Varying the catalyst loading between 0.1 and 0.2 equivalents showed negligible impact on the catalytic process (entries 5–8), with yields consistently over 80%. It is important to note that although  $\text{DSEACl}_2$  and  $\text{PbI}_2$  salts are capable of absorbing visible light in the blue light region (Fig. S6), the control reactions using these two light absorbers yield only 51% ( $\text{DSEACl}_2$ , entry 9) and  $< 5\%$  of product ( $\text{PbI}_2$ , entry 10) under the same operating conditions,

**Table 1** Optimization of reaction conditions for selective reduction of unsaturated ketones



Entry <sup>a</sup>	$\lambda_{\text{ex}}$ (nm)	Catalyst (equiv.)	Solvent	Yield <sup>b</sup> (%)
1	450	$(\text{SEA})_2\text{PbI}_4$ (0.20)	Isopropanol	56
2	450	$(\text{SEA})_2\text{PbI}_4$ (0.20)	Toluene	46
3	450	$(\text{SEA})_2\text{PbI}_4$ (0.20)	Chloroform	33
4	450	$(\text{SEA})_2\text{PbI}_4$ (0.20)	Acetonitrile	29
5	450	$(\text{SEA})_2\text{PbI}_4$ (0.20)	Hexanes	81
6	450	$(\text{SEA})_2\text{PbI}_4$ (0.15)	Hexanes	82
7	450	$(\text{SEA})_2\text{PbI}_4$ (0.10)	Hexanes	85
8	450	$(\text{SEA})_2\text{PbI}_4$ (0.05)	Hexanes	34
9	450	$\text{DSEACl}_2$ (0.10)	Hexanes	51
10	450	$\text{PbI}_2$ (0.10)	Hexanes	Trace
11	—	$(\text{SEA})_2\text{PbI}_4$ (0.10)	Hexanes	Trace
12	525	$(\text{SEA})_2\text{PbI}_4$ (0.10)	Hexanes	87
13	525	$\text{DSEACl}_2$ (0.10)	Hexanes	33
14	525	$\text{PbI}_2$ (0.10)	Hexanes	Trace
15	450/525	—	Hexanes	Trace

<sup>a</sup> Conditions: substrate **1a** (0.1 mmol),  $\text{H}_3\text{PO}_2$  (0.12 mmol, 50 wt%),  $(\text{SEA})_2\text{PbI}_4$ , solvent (2.0 mL),  $\text{N}_2$ , 60 °C, 16 h, under LED illumination.

<sup>b</sup> Refers to  $^1\text{H}$  NMR yield, which is calculated using 1,3,5-trimethoxybenzene as the internal standard.

indicating the importance of the coexistence of selenol groups and lead halide units within a TMHP structure for boosting the photocatalytic efficiency.

We next investigated the irradiation-dependent reactivity of the TMHP catalyst. Control experiments in the dark showed negligible chalcone conversion (entry 11), indicating the necessity of irradiation. Favored by the absorption spectrum of  $(\text{SEA})_2\text{PbI}_4$  in the broad regions shorter than 548 nm, the reaction can be driven by blue ( $\lambda_{\text{ex}} = 450$  nm) and green ( $\lambda_{\text{ex}} = 525$  nm) light with high product yield (85% and 87%, respectively, entries 7 and 12). In contrast, the control reactions using  $\text{DSEACl}_2$  as the catalyst decreased from 51% under blue light to 33% (entry 13), suggesting more efficient charge separation and transfer in  $(\text{SEA})_2\text{PbI}_4$  under visible-light irradiation induced by the incorporation of lead halide layers.

### Substrate scope for the reduction of $\alpha,\beta$ -unsaturated ketones

We further evaluated the substrate scope with the optimized reaction conditions (Fig. 3 and S7–S47). All chalcones, regardless of whether they contained electron-donating (**2b–2e**) or electron-withdrawing (**2f–2j**) substituents on the phenyl ring, were successfully reduced with isolated yields ranging from 37% to 81%. A clear electronic trend was observed: substrates bearing electron-donating groups afforded higher yields (e.g., **2b**: 81%; **2c**: 78%), while those with electron-withdrawing groups gave comparatively lower yields (**2f–2j**: 37–67%). This trend is consistent with the proposed radical-mediated mechanism, where electron-donating substituents stabilize the key radical-cation intermediate, thereby facilitating the reduction. Notably, for substrates containing multiple unsaturated bonds



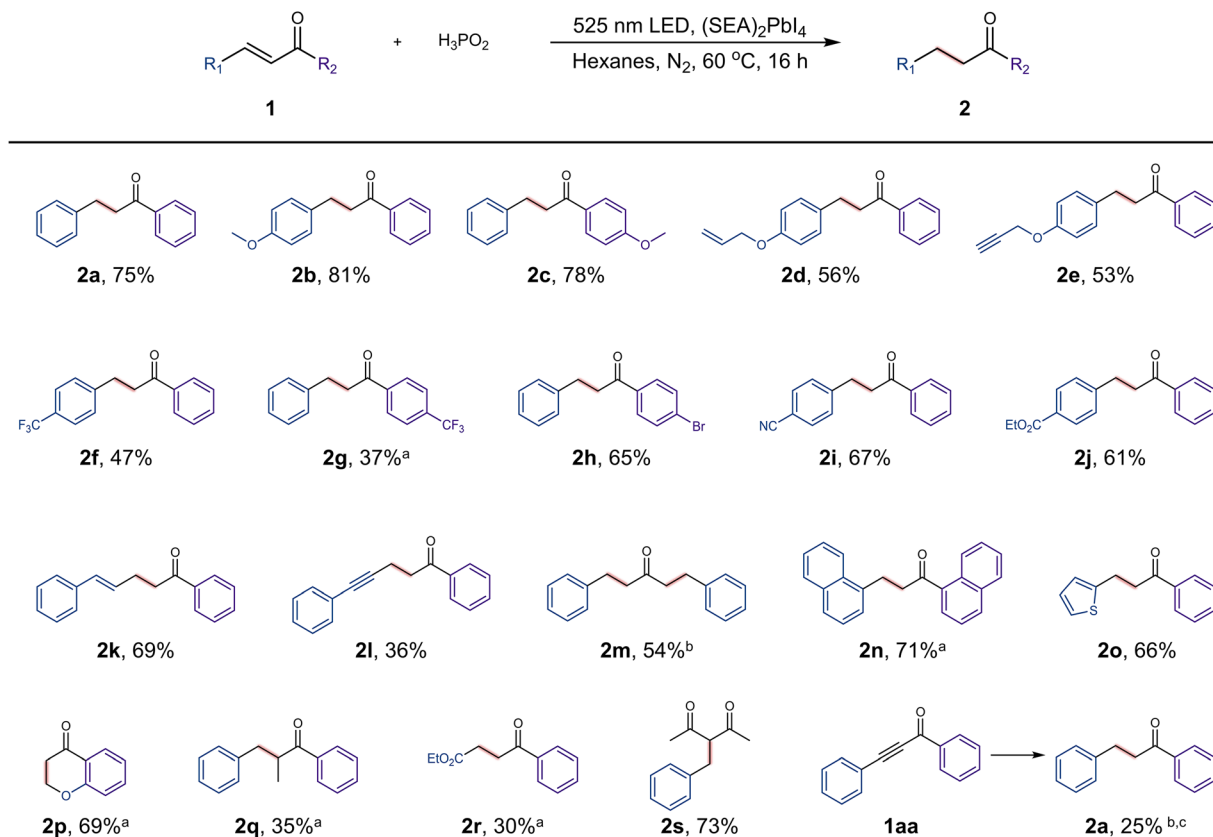


Fig. 3 Substrate scope of photocatalytic reduction with various ketone structures. Reaction conditions: substrate **1** (0.1 mmol),  $\text{H}_3\text{PO}_2$  (0.12 mmol, 50 wt%),  $(\text{SEA})_2\text{PbI}_4$  (0.01 mmol), hexane (2.0 mL),  $\text{N}_2$ , 60 °C, 16 h, under 525 nm LED illumination. Yields were isolated yields. <sup>a</sup>Reaction time: 36 h. <sup>b</sup> $\text{H}_3\text{PO}_2$  (0.22 mmol). <sup>c</sup>Acetylene ketone **1aa** can also be reduced to **2a** under these conditions.

(e.g., with terminal allyl (**1d**) and propargyl (**1e**) groups on the aryl ring, or conjugated  $\alpha,\beta,\gamma,\delta$ -unsaturated structures (**1k** and **1l**)), the reduction occurred selectively at the C=C bond in the  $\alpha,\beta$ -unsaturated site with isolated yields from 36% to 69%, while other unsaturated bonds were preserved (Fig. 3). We ascribe the high chemoselectivity to the polarization effect arising from conjugation with the carbonyl group, which renders the  $\beta$ -carbon partially positively charged. The nucleophilic selenium atom on the surface of  $(\text{SEA})_2\text{PbI}_4$  therefore can attack the  $\beta$ -carbon *via* a 1,4-conjugate addition pathway, forming a  $\beta$ -seleno carbonyl intermediate that can subsequently undergo further reduction. Moreover, substrates with  $\alpha,\beta$ -unsaturated C=C bonds on both sides of the central carbonyl (e.g., biphenylpentadienone (**1m**)) can be completely reduced to form fully saturated ketones with a considerably high yield of 54%, indicating the capability of multi-site activation with photoexcited  $(\text{SEA})_2\text{PbI}_4$ . The selective reduction is found to be effective for extended types of substrates such as a naphthyl substituent (**1n**), heterocycles (**1o** and **1p**), a sterically hindered  $\alpha$ -substituted substrate (**1q**), an ester group (**1r**), a diketone (**1s**), and an aromatic alkynyl ketone (**1aa**), with isolated yields ranging from 30% to 73%.

### Mechanistic studies on the TMHP-driven photocatalytic reactions

To gain mechanistic insight into the selective reduction of unsaturated ketones better, related control experiments were conducted. First, excess equivalents of radical scavenger 2,2,6,6-tetramethylpiperidine-1-oxyl (TEMPO) were added to the catalytic system (Fig. 4a). We found that the formation of the product was inhibited significantly, regardless of whether  $(\text{SEA})_2\text{PbI}_4$  or  $\text{DSEACl}_2$  was used as the catalyst, indicating that radical species might be involved in the catalytic reduction process.

To investigate the role of irradiation in the catalytic process, we next conducted control experiments without irradiation and collected the solid and liquid to analyze the progress of the reaction. Only a negligible amount of product (yield below 2%) was detected from the solution after a 16-h reaction in the dark, while the  $\beta$ -seleno carbonyl intermediates were observed in solid-phase residues when either  $(\text{SEA})_2\text{PbI}_4$  or  $\text{DSEACl}_2$  was used in stoichiometric amounts, as confirmed by NMR and mass spectrometry (MS) studies of the isolated solid residues (Fig. 4b and S48–S50). These results hint at the 1,4-addition on the  $\alpha,\beta$ -unsaturated moiety between the selenol groups and the chalcone substrate even in the absence of light, consistent with the previous reports.<sup>71,72,74</sup> These results indicate that light is not required for the formation of the  $\beta$ -seleno carbonyl



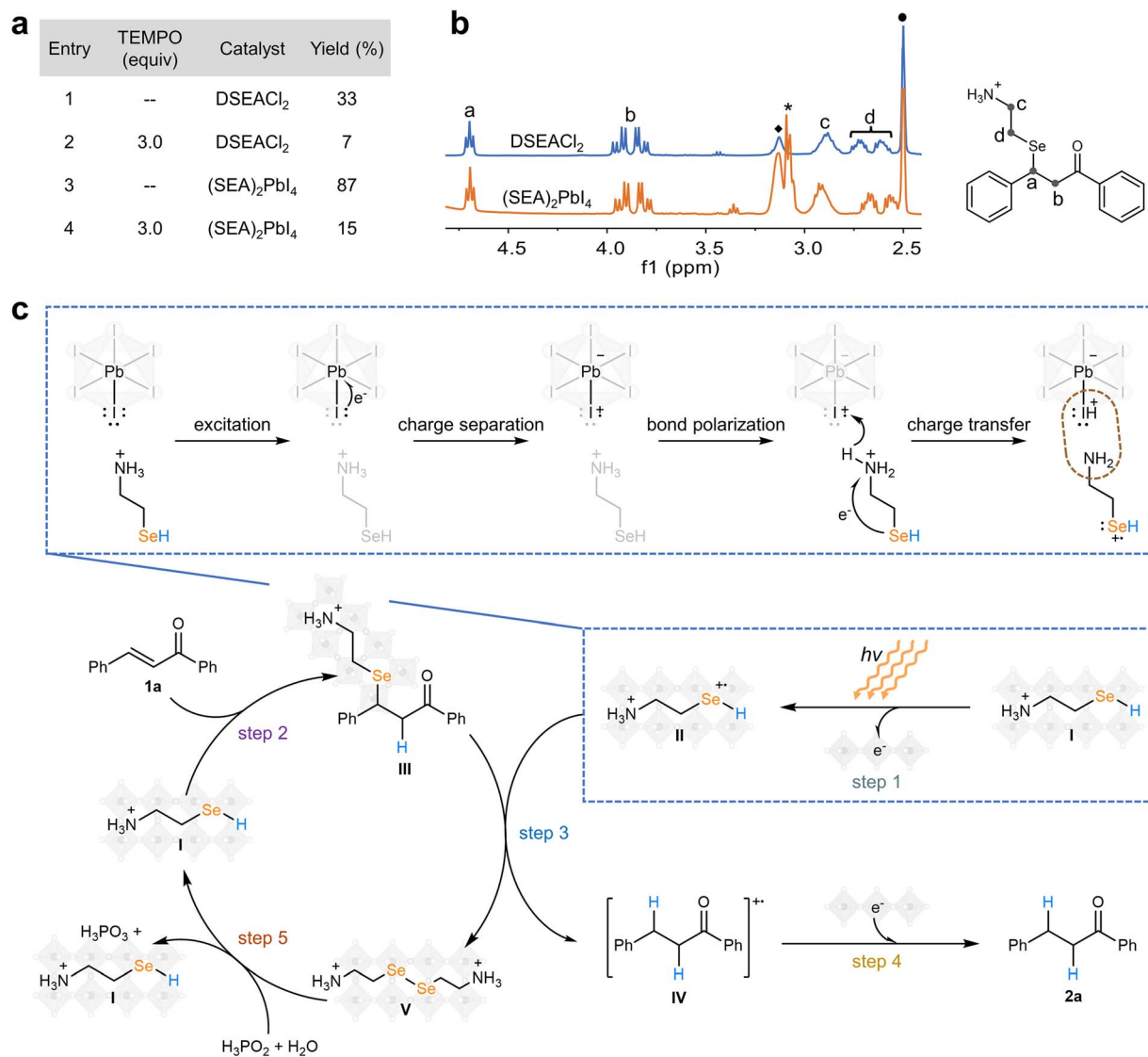


Fig. 4 Mechanistic investigation of TMHP-promoted photocatalytic reduction. (a) Inhibition of the reaction by the application of TEMPO as a radical trap. (b) <sup>1</sup>H NMR spectra (400 MHz, DMSO-*d*<sub>6</sub>) of the solid residues from reactions of chalcone **1a** with stoichiometric amounts of DSEACl<sub>2</sub> (blue line) or (SEA)<sub>2</sub>PbI<sub>4</sub> (orange line) under standard reaction conditions but in the dark. The residual solvent DMSO, the trace amount of water, and unknown impurities are denoted using a circle (●), a black diamond (◆), and an asterisk (\*), respectively. (c) Proposed mechanism for (SEA)<sub>2</sub>PbI<sub>4</sub>-catalyzed selective reduction of  $\alpha,\beta$ -unsaturated ketones using chalcone as the model substrate: under irradiation, (SEA)<sub>2</sub>PbI<sub>4</sub> (I) generates photoinduced charge carriers, which undergo intramolecular transfer to form surface-bound selenium radicals (II) (step 1, detailed sub-steps are shown in the blue dashed box). Meanwhile, the chalcone (**1a**) undergoes 1,4-addition with the surface-bound selenol species (II), forming the  $\beta$ -seleno carbonyl intermediate (III) (step 2); the as-formed selenium radical (II) further promotes the cleavage of the Se–C bond on TMHP surfaces (III) to generate the radical cation intermediate (IV) and diselenide species (V) (step 3); the intermediate (IV) is finally reduced by the photoexcited TMHPs to yield the saturated product (**2a**) (step 4), while the diselenide is recycled to selenium species by H<sub>3</sub>PO<sub>2</sub>/H<sub>2</sub>O (step 5) to complete the catalytic cycle.

intermediate but rather functions as an excitation source absorbed by the TMHP to generate excitons that drive the subsequent reduction steps.

A standard hot filtration test was carried out to evaluate the heterogeneous nature of the TMHP catalysis. After removal of the solid catalyst at the reaction temperature, the filtrate was further irradiated under identical conditions. <sup>1</sup>H NMR analysis showed that the product yield remained virtually unchanged, increasing only from 20% to 21% (Fig. S51), demonstrating that

no catalytically active species leach into solution and confirming the heterogeneous nature of the TMHP catalysis.

The material characterization and mechanistic studies lead us to a more detailed model of the TMHP-promoted photocatalytic process (Fig. 4c). Upon irradiation, the inorganic [PbI<sub>4</sub>]<sup>2-</sup> layer of (SEA)<sub>2</sub>PbI<sub>4</sub> (I) absorbs photons, generating electron-hole pairs, with the electron and hole becoming localized on the Pb and I atoms of the inorganic framework, respectively. The hole residing on the I atom renders it electron-



deficient. This electron-deficient I atom can abstract an electron from the nearby Se–H group *via* the hydrogen-bonding network, given that Se is the most electropositive site in the organic cation. This leads to the oxidation of selenol, yielding selenyl radical cations (**II**) as the intermediate species (step 1).

Meanwhile, the unsaturated ketone molecule (taking chalcone (**1a**) for example) undergoes nucleophilic 1,4-conjugate addition with the surface-bound selenol species (**I**), forming the intermediate (**III**), which is a spontaneous reaction (step 2,  $\Delta G_1 = -11.3 \text{ kcal mol}^{-1}$ , Scheme S1). Subsequently, **III** interacts with the surface selenyl radical cation (**II**, formed *in situ* from the visible light excitation process as shown in Fig. 4c) and triggers exothermic heterolytic Se–C cleavage (step 3,  $\Delta G_2 = -16.0 \text{ kcal mol}^{-1}$ ), yielding radical-cation-containing intermediate **IV**, accompanied by the release of the diselenide structure (**V**). Subsequent electron transfer from the photoexcited inorganic layer reduces **IV** to the saturated product **2a**, completing the selective reduction (step 4) with  $\Delta G_3 = -13.6 \text{ kcal mol}^{-1}$ . With the presence of  $\text{H}_2\text{O}$  and  $\text{H}_3\text{PO}_2$ , diselenide (**V**) is reduced to form selenol-containing **I** and completes the catalytic cycle (step 5).

It is important to note, however, that a primary limitation of this system is the participation of only surface-exposed selenol ligands in the catalytic cycle. The progressive loss of these SEA groups through repeated redox cycling results in gradual degradation of the TMHP catalyst (Fig. S52 and S53). This is consistent with the catalytic recycling experiments, which show a gradual decrease in product yield from 87% in the first cycle to 13% after four cycles (Fig. S54). Future improvements in reaction parameters, such as the rational design of new selenol-containing cations and optimization of the solvent environment, are expected to enhance the stability of TMHP-based materials and broaden their utility in heterogeneous catalytic reactions.

## Conclusions

In this work, we have developed a new photocatalyst design by integrating selenol-containing organic cations into two-dimensional metal halide perovskites (TMHPs), creating a unified crystalline platform  $(\text{SEA})_2\text{PbI}_4$  that combines efficient light absorption, charge carrier generation and separation, and catalytic activation. The hybrid framework demonstrates notable stability for typically labile Se–H bonds and enables visible-light-driven selective reduction of  $\alpha,\beta$ -unsaturated ketones with a broad substrate scope and high chemoselectivity. Mechanistic investigations reveal a radical-mediated pathway in which photoexcited charges from the inorganic layers activate selenol groups to promote selective reduction reactions on various types of unsaturated carbonyl compounds, highlighting the unique synergy between perovskite photo-physics and incorporated molecular catalysis. This work advances the fundamental understanding of TMHP-based photocatalysis and provides a general design strategy for multifunctional perovskite materials. By overcoming traditional limitations of charge recombination and lattice mismatches, our approach opens new possibilities for applying perovskites in light-driven selective organic transformations and chemical synthesis.

## Author contributions

W. L. and L. L. contributed equally. W. L. and Z. Y. designed the study and wrote the paper. W. L. synthesized and characterized the TMHPs. W. L., L. L., J. L. (Jingpeng Li), W. Q., and X. Z. conducted the catalytic experiments. J. L. (Jialong Liu) prepared the carbonyl substrates. Y. Z., G. Y., and T. Z. performed the computational studies. All authors approved the final version of the manuscript.

## Conflicts of interest

A provisional patent application CN119059949A was filed on December 3, 2024 by Sun Yat-sen University. The remaining authors declare no competing interests.

## Data availability

CCDC 2348172 contains the supplementary crystallographic data for this paper.<sup>76</sup>

The data supporting the findings of this study are available in the article and its supplementary information (SI) or from the corresponding authors upon reasonable request. Supplementary information: materials and methods, additional structural and optical characterization, substrate synthetic procedures, summary of NMR data, and supplementary mechanistic studies. See DOI: <https://doi.org/10.1039/d5sc09706a>.

## Acknowledgements

All calculations were carried out using the Tianhe-2 (TH-2) super computer clusters (Guangzhou, Guangdong, China) and resources provided by Digital Research Alliance of Canada. Z. Y. would like to acknowledge financial support from the National Natural Science Foundation of China (no. 21905316, 22175201, and 22475239), the Department of Science and Technology of Guangdong Province (no. 2019QN01C108), and Sun Yat-sen University. T. Z. thanks the Natural Sciences and Engineering Research Council (NSERC) of Canada (no. RGPIN-2024-06286) for financial support. All single crystal X-ray diffraction tests were conducted by the Testing Center of Sun Yat-sen University. X. Z. would like to acknowledge financial support from the National Natural Science Foundation of China (no. 22171292 and 22371308). L. L. thanks the Guangzhou Science and Technology Plan, Basic and Applied Basic Research Special Topic, Young Doctoral “Sailing” Project (no. 2025A04J4290), and the Fundamental Research Funds for the Central Universities, Sun Yat-sen University (no. 24qnpy048) for financial support.

## References

- B. Saporov and D. B. Mitzi, Organic–Inorganic Perovskites: Structural Versatility for Functional Materials Design, *Chem. Rev.*, 2016, **116**, 4558–4596.
- T. M. Brenner, D. A. Egger, L. Kronik, G. Hodes and D. Cahen, Hybrid organic–inorganic perovskites: low-cost



- semiconductors with intriguing charge-transport properties, *Nat. Rev. Mater.*, 2016, **1**, 15007.
- 3 L. N. Quan, B. P. Rand, R. H. Friend, S. G. Mhaisalkar, T.-W. Lee and E. H. Sargent, Perovskites for Next-Generation Optical Sources, *Chem. Rev.*, 2019, **119**, 7444–7477.
  - 4 J. L. Knutson, J. D. Martin and D. B. Mitzi, Tuning the Band Gap in Hybrid Tin Iodide Perovskite Semiconductors Using Structural Templating, *Inorg. Chem.*, 2005, **44**, 4699–4705.
  - 5 X. Li, J. M. Hoffman and M. G. Kanatzidis, The 2D Halide Perovskite Rulebook: How the Spacer Influences Everything from the Structure to Optoelectronic Device Efficiency, *Chem. Rev.*, 2021, **121**, 2230–2291.
  - 6 J. Han, K. Park, S. Tan, Y. Vaynzof, J. Xue, E. W.-G. Diau, M. G. Bawendi, J.-W. Lee and I. Jeon, Perovskite solar cells, *Nat. Rev. Methods Primers*, 2025, **5**, 3.
  - 7 S. Park, W. J. Chang, C. W. Lee, S. Park, H.-Y. Ahn and K. T. Nam, Photocatalytic hydrogen generation from hydriodic acid using methylammonium lead iodide in dynamic equilibrium with aqueous solution, *Nat. Energy*, 2016, **2**, 16185.
  - 8 Y. Wu, P. Wang, X. Zhu, Q. Zhang, Z. Wang, Y. Liu, G. Zou, Y. Dai, M. H. Whangbo and B. Huang, Composite of  $\text{CH}_3\text{NH}_3\text{PbI}_3$  with Reduced Graphene Oxide as a Highly Efficient and Stable Visible-Light Photocatalyst for Hydrogen Evolution in Aqueous HI Solution, *Adv. Mater.*, 2018, **30**, 1704342.
  - 9 Y. Wu, P. Wang, Z. Guan, J. Liu, Z. Wang, Z. Zheng, S. Jin, Y. Dai, M.-H. Whangbo and B. Huang, Enhancing the Photocatalytic Hydrogen Evolution Activity of Mixed-Halide Perovskite  $\text{CH}_3\text{NH}_3\text{PbBr}_{3-x}\text{I}_x$  Achieved by Bandgap Funneling of Charge Carriers, *ACS Catal.*, 2018, **8**, 10349–10357.
  - 10 Y.-F. Xu, M.-Z. Yang, B.-X. Chen, X.-D. Wang, H.-Y. Chen, D.-B. Kuang and C.-Y. Su, A  $\text{CsPbBr}_3$  Perovskite Quantum Dot/Graphene Oxide Composite for Photocatalytic  $\text{CO}_2$  Reduction, *J. Am. Chem. Soc.*, 2017, **139**, 5660–5663.
  - 11 M. Ou, W. Tu, S. Yin, W. Xing, S. Wu, H. Wang, S. Wan, Q. Zhong and R. Xu, Amino-Assisted Anchoring of  $\text{CsPbBr}_3$  Perovskite Quantum Dots on Porous  $\text{g-C}_3\text{N}_4$  for Enhanced Photocatalytic  $\text{CO}_2$  Reduction, *Angew. Chem., Int. Ed.*, 2018, **57**, 13570–13574.
  - 12 Y. Jiang, J.-F. Liao, Y.-F. Xu, H.-Y. Chen, X.-D. Wang and D.-B. Kuang, Hierarchical  $\text{CsPbBr}_3$  nanocrystal-decorated  $\text{ZnO}$  nanowire/macroporous graphene hybrids for enhancing charge separation and photocatalytic  $\text{CO}_2$  reduction, *J. Mater. Chem. A*, 2019, **7**, 13762–13769.
  - 13 Y. Jiang, J.-F. Liao, H.-Y. Chen, H.-H. Zhang, J.-Y. Li, X.-D. Wang and D.-B. Kuang, All-Solid-State Z-Scheme  $\alpha\text{-Fe}_2\text{O}_3/\text{Amine-RGO}/\text{CsPbBr}_3$  Hybrids for Visible-Light-Driven Photocatalytic  $\text{CO}_2$  Reduction, *Chem*, 2020, **6**, 766–780.
  - 14 X. Zhu, Y. Lin, Y. Sun, M. C. Beard and Y. Yan, Lead-Halide Perovskites for Photocatalytic  $\alpha$ -Alkylation of Aldehydes, *J. Am. Chem. Soc.*, 2019, **141**, 733–738.
  - 15 K. Wang, H. Lu, X. Zhu, Y. Lin, M. C. Beard, Y. Yan and X. Chen, Ultrafast Reaction Mechanisms in Perovskite Based Photocatalytic C–C Coupling, *ACS Energy Lett.*, 2020, **5**, 566–571.
  - 16 Y. Feng, D. Chen, M. Niu, Y. Zhong, H. Ding, Y. Hu, X. Wu and Z. Yuan, Recent progress in metal halide perovskite-based photocatalysts: physicochemical properties, synthetic strategies, and solar-driven applications, *J. Mater. Chem. A*, 2023, **11**, 22058–22086.
  - 17 H. Huang, H. Yuan, K. P. F. Janssen, G. Solís-Fernández, Y. Wang, C. Y. X. Tan, D. Jonckheere, E. Debroye, J. Long, J. Hendrix, J. Hofkens, J. A. Steele and M. B. J. Roeffaers, Efficient and Selective Photocatalytic Oxidation of Benzylic Alcohols with Hybrid Organic–Inorganic Perovskite Materials, *ACS Energy Lett.*, 2018, **3**, 755–759.
  - 18 A. L. Linsebigler, G. Lu and J. T. Yates, Jr., Photocatalysis on  $\text{TiO}_2$  Surfaces: Principles, Mechanisms, and Selected Results, *Chem. Rev.*, 1995, **95**, 69–96.
  - 19 N. Serpone and A. V. Emeline, Semiconductor Photocatalysis—Past, Present, and Future Outlook, *J. Phys. Chem. Lett.*, 2012, **3**, 673–677.
  - 20 L. Zhang, J. Ran, S.-Z. Qiao and M. Jaroniec, Characterization of semiconductor photocatalysts, *Chem. Soc. Rev.*, 2019, **48**, 5184–5206.
  - 21 X. Zhu, Y. Lin, J. San Martin, Y. Sun, D. Zhu and Y. Yan, Lead halide perovskites for photocatalytic organic synthesis, *Nat. Commun.*, 2019, **10**, 2843.
  - 22 J. T. DuBose and P. V. Kamat, Surface Chemistry Matters. How Ligands Influence Excited State Interactions between  $\text{CsPbBr}_3$  and Methyl Viologen, *J. Phys. Chem. C*, 2020, **124**, 12990–12998.
  - 23 Y. Yuan, H. Zhu, K. Hills-Kimball, T. Cai, W. Shi, Z. Wei, H. Yang, Y. Candler, P. Wang, J. He and O. Chen, Stereoselective C–C Oxidative Coupling Reactions Photocatalyzed by Zwitterionic Ligand Capped  $\text{CsPbBr}_3$  Perovskite Quantum Dots, *Angew. Chem., Int. Ed.*, 2020, **59**, 22563–22569.
  - 24 A. Kipkorir, J. DuBose, J. Cho and P. V. Kamat,  $\text{CsPbBr}_3\text{-CdS}$  heterostructure: stabilizing perovskite nanocrystals for photocatalysis, *Chem. Sci.*, 2021, **12**, 14815–14825.
  - 25 J. T. DuBose and P. V. Kamat, Efficacy of Perovskite Photocatalysis: Challenges to Overcome, *ACS Energy Lett.*, 2022, **7**, 1994–2011.
  - 26 Z.-Y. Chen, N.-Y. Huang and Q. Xu, Metal halide perovskite materials in photocatalysis: Design strategies and applications, *Coordin. Chem. Rev.*, 2023, **481**, 215031.
  - 27 H. Tong, F. F. Li, M. Du, H. Song, B. Han, G. Jia, X. Q. Xu, X. Zou, L. Ji, J. J. Kai, Z. Hu and H. Y. Hsu, Interface Engineering, Charge Carrier Dynamics, and Solar-Driven Applications of Halide Perovskite/2D Material Heterostructured Photocatalysts, *ACS Appl. Mater. Interfaces*, 2025, **17**, 23431–23465.
  - 28 J. Low, J. Yu, M. Jaroniec, S. Wageh and A. A. Al-Ghamdi, Heterojunction Photocatalysts, *Adv. Mater.*, 2017, **29**, 1601694.
  - 29 B. J. Ng, L. K. Putri, X. Y. Kong, Y. W. Teh, P. Pasbakhsh and S. P. Chai, Z-Scheme Photocatalytic Systems for Solar Water Splitting, *Adv. Sci.*, 2020, **7**, 1903171.



- 30 Y.-J. Chen, Y.-M. Xu, X.-L. Ye, Z.-P. Luo, S.-P. Zhu, K.-F. Li, J.-F. Lu, G.-E. Wang and G. Xu, Strategic energy-level modulation in porous heterojunctions: advancing gas sensing through Type-I to Type-II transitions, *Nat. Commun.*, 2025, **16**, 6634.
- 31 L. Zhang, J. Zhang, J. Yu and H. García, Charge-transfer dynamics in S-scheme photocatalyst, *Nat. Rev. Chem.*, 2025, **9**, 328–342.
- 32 Z. Ning, X. Gong, R. Comin, G. Walters, F. Fan, O. Voznyy, E. Yassitepe, A. Buin, S. Hoogland and E. H. Sargent, Quantum-dot-in-perovskite solids, *Nature*, 2015, **523**, 324–328.
- 33 X. Gong, Z. Yang, G. Walters, R. Comin, Z. Ning, E. Beauregard, V. Adinolfi, O. Voznyy and E. H. Sargent, Highly efficient quantum dot near-infrared light-emitting diodes, *Nat. Photonics*, 2016, **10**, 253–257.
- 34 J. Liu and J. Zhang, Nanointerface Chemistry: Lattice-Mismatch-Directed Synthesis and Application of Hybrid Nanocrystals, *Chem. Rev.*, 2020, **120**, 2123–2170.
- 35 L. Ruan and Y. Zhang, NIR-excitable heterostructured upconversion perovskite nanodots with improved stability, *Nat. Commun.*, 2021, **12**, 219.
- 36 H. Xiao, B. Liu, L. Qiu, G. Li, G. Zhang, D. Huang, Y. Zhao, C. Yang, F. Jiang, P. Dang, H. Lian, Z. Cheng and J. Lin, Core-Shell Structured Upconversion/Lead-Free Perovskite Nanoparticles for Anticounterfeiting Applications, *Angew. Chem., Int. Ed.*, 2021, **61**, e202115136.
- 37 X. Shi, W. Dai, X. Li, Z. Zhu, X. a. Dong and Z. Cui, Lattice-Matched S-Scheme High-Entropy Oxide Heterojunction for Efficient Visible-light-Driven CO<sub>2</sub> Photomethanation, *Adv. Funct. Mater.*, 2025, **35**, e11696.
- 38 Z. Yu, W. K. Chan, D. Zhou, X. Li, Y. Lu, Z. Jiang, B. Xue, H. Zhu, S. Dowland, J. Ye, A. Tew, L. van Turnhout, Q. Gu, L. Dai, T. Liu, C. Ducati, A. Rao and T. T. Y. Tan, Overcoming lattice mismatch for core-shell NaGdF<sub>4</sub>@CsPbBr<sub>3</sub> heterostructures, *Nat. Commun.*, 2025, **16**, 3891.
- 39 Z. Yuan, L. Zhao, E. Pradhan, M. Lai, T. Zeng and Z. Yang, Postsynthetic Crystalline Transformation in Two-Dimensional Perovskites via Organothioliol-Based Chemistry, *CCS Chem.*, 2022, **4**, 855–863.
- 40 W. Li, J. He, Y. Zhang, L. Ye, G. Yao, Z. Zhang, S. Li, X. Lu, H. Lu, T. Zeng and Z. Yang, Branched intercalating cations regulate the structural evolution of two-dimensional perovskites, *Cell Rep. Phys. Sci.*, 2025, **6**, 102509.
- 41 Y. Fu, W. Zheng, X. Wang, M. P. Hautzinger, D. Pan, L. Dang, J. C. Wright, A. Pan and S. Jin, Multicolor Heterostructures of Two-Dimensional Layered Halide Perovskites that Show Interlayer Energy Transfer, *J. Am. Chem. Soc.*, 2018, **140**, 15675–15683.
- 42 E. S. Akriti, S. B. Shiring, J. Yang, C. L. Atencio-Martinez, B. Yuan, X. Hu, Y. Gao, B. P. Finkenauer, A. J. Pistone, Y. Yu, P. Liao, B. M. Savoie and L. Dou, Layer-by-layer anionic diffusion in two-dimensional halide perovskite vertical heterostructures, *Nat. Nanotech.*, 2021, **16**, 584–591.
- 43 Z. Ou, C. Wang, Z. G. Tao, Y. Li, Z. Li, Y. Zeng, Y. Li, E. Shi, W. Chu, T. Wang and H. Xu, Organic Ligand Engineering for Tailoring Electron-Phonon Coupling in 2D Hybrid Perovskites, *Nano Lett.*, 2024, **24**, 5975–5983.
- 44 L. Romani, A. Bala, V. Kumar, A. Speltini, A. Milella, F. Fracassi, A. Listorti, A. Profumo and L. Malavasi, PEA<sub>2</sub>SnBr<sub>4</sub>: a water-stable lead-free two-dimensional perovskite and demonstration of its use as a co-catalyst in hydrogen photogeneration and organic-dye degradation, *J. Mater. Chem. C*, 2020, **8**, 9189–9194.
- 45 H. Fu, X. Liu, J. Fu, Y. Wu, Q. Zhang, Z. Wang, Y. Liu, Z. Zheng, H. Cheng, Y. Dai, B. Huang and P. Wang, 2D/Quasi-2D Ruddlesden-Popper Perovskite: A High-Performance Photocatalyst for Hydrogen Evolution, *ACS Catal.*, 2023, **13**, 14716–14724.
- 46 Z.-J. Bai, J. Xiong, Y. Mao, S. Tian, B.-H. Wang, B. Hu, X. Wang, W. Zhou, C.-T. Au, L. Chen and S.-F. Yin, Lead-free Dion-Jacobson layered double perovskite as a photocatalyst for toluene oxidation, *Cell Rep. Phys. Sci.*, 2023, **4**, 101591.
- 47 Y. Peng, Y. Zhang, X. Wang, X. Y. Sui, M. Y. Lin, Y. Zhu, C. Jing, H. Y. Yuan, S. Yang, P. F. Liu, S. Dai, Z. Zheng, H. G. Yang and Y. Hou, Polar Aromatic Two-dimensional Dion-Jacobson Halide Perovskites for Efficient Photocatalytic H<sub>2</sub> Evolution, *Angew. Chem., Int. Ed.*, 2024, **63**, e202319882.
- 48 J. Kaur and S. C. Peter, Two-Dimensional Perovskites for Photocatalytic CO<sub>2</sub> Reduction, *Angew. Chem., Int. Ed.*, 2025, **64**, e202418708.
- 49 N. Mercier, S. Poiroux, A. Riou and P. Batail, Unique Hydrogen Bonding Correlating with a Reduced Band Gap and Phase Transition in the Hybrid Perovskites (HO(CH<sub>2</sub>)<sub>2</sub>NH<sub>3</sub>)<sub>2</sub>PbX<sub>4</sub> (X = I, Br), *Inorg. Chem.*, 2004, **43**, 8361–8366.
- 50 J. V. Smith and J. M. Bennett, Hydroxyl Groups in Zeolite Catalysts, *Nature*, 1968, **219**, 1040–1041.
- 51 Y. Peng, L. Wang, Q. Luo, Y. Cao, Y. Dai, Z. Li, H. Li, X. Zheng, W. Yan, J. Yang and J. Zeng, Molecular-Level Insight into How Hydroxyl Groups Boost Catalytic Activity in CO<sub>2</sub> Hydrogenation into Methanol, *Chem*, 2018, **4**, 613–625.
- 52 D. Pakulski, V. Montes-García, A. Gorczyński, W. Czepa, T. Chudziak, P. Samori and A. Ciesielski, Thiol-decorated covalent organic frameworks as multifunctional materials for high-performance supercapacitors and heterogeneous catalysis, *J. Mater. Chem. A*, 2022, **10**, 16685–16696.
- 53 X. Bao, W. Yu and G. Wang, Thiols as Powerful Atom Transfer Catalyst: Opportunities in Photoredox-Mediated Reactions, *Adv. Synth. Catal.*, 2023, **365**, 2299–2309.
- 54 G. S. Phun, H. S. Slocumb, K. J. Ruud, S. Nie, C. Antonio, F. Furche, V. M. Dong and X.-H. Yang, Hydroselenation of olefins: elucidating the β-selenium effect, *Chem. Sci.*, 2024, **15**, 20523–20533.
- 55 A. Capperucci, A. Petrucci, C. Faggi and D. Tanini, Click Reaction of Selenols with Isocyanates: Rapid Access to Selenocarbamates as Peroxide-Switchable Reservoir of Thiol-Peroxidase-Like Catalysts, *Adv. Synth. Catal.*, 2021, **363**, 4256–4263.



- 56 D. Tanini and A. Capperucci, Synthesis and Applications of Organic Selenols, *Adv. Synth. Catal.*, 2021, **363**, 5360–5385.
- 57 W. H. H. Günther, Hypophosphorous Acid, a Novel Reagent for the Reduction of Diselenides and the Selenol-Catalyzed Reduction of Disulfides, *J. Org. Chem.*, 1966, **31**, 1202–1205.
- 58 R. S. Rowland and R. Taylor, Intermolecular Nonbonded Contact Distances in Organic Crystal Structures: Comparison with Distances Expected from van der Waals Radii, *J. Phys. Chem.*, 1996, **100**, 7384–7391.
- 59 L. Mao, W. Ke, L. Pedesseau, Y. Wu, C. Katan, J. Even, M. R. Wasielewski, C. C. Stoumpos and M. G. Kanatzidis, Hybrid Dion–Jacobson 2D Lead Iodide Perovskites, *J. Am. Chem. Soc.*, 2018, **140**, 3775–3783.
- 60 L. Mao, C. C. Stoumpos and M. G. Kanatzidis, Two-dimensional hybrid halide perovskites: principles and promises, *J. Am. Chem. Soc.*, 2019, **141**, 1171–1190.
- 61 L. Zhao, Y. Zhang, H. Chen, T. Zeng and Z. Yang, Two-Dimensional Lead Halide Perovskites with Spirocyclic Intercalating Cations, *Chem. Mater.*, 2024, **36**, 5788–5795.
- 62 P. C. Nam and M. T. Nguyen, The Se–H bond of benzeneselenols (ArSe–H): Relationship between bond dissociation enthalpy and spin density of radicals, *Chem. Phys.*, 2013, **415**, 18–25.
- 63 A. B. Harvey and M. K. Wilson, Vibrational Spectrum of Methaneselenol, *J. Chem. Phys.*, 1966, **45**, 678–688.
- 64 N. Sharghi and I. Lalezari, The infrared absorption spectra of selenomercaptans and selenols, *Spectrochim. Acta*, 1964, **20**, 237–238.
- 65 Y. Fang, L. Zhang, Y. Yu, X. Yang, K. Wang and B. Zou, Manipulating Emission Enhancement and Piezochromism in Two-Dimensional Organic-Inorganic Halide Perovskite  $[(\text{HO})(\text{CH}_2)_2\text{NH}_3]_2\text{PbI}_4$  by High Pressure, *CCS Chem.*, 2021, **3**, 2203–2210.
- 66 D. Tanini, S. Scarpelli, E. Ermini and A. Capperucci, Seleno-Michael Reaction of Stable Functionalised Alkyl Selenols: A Versatile Tool for the Synthesis of Acyclic and Cyclic Unsymmetrical Alkyl and Vinyl Selenides, *Adv. Synth. Catal.*, 2019, **361**, 2337–2346.
- 67 H. S. Slocumb, S. Nie, V. M. Dong and X.-H. Yang, Enantioselective Selenol-ene Using Rh-Hydride Catalysis, *J. Am. Chem. Soc.*, 2022, **144**, 18246–18250.
- 68 E. Li, J. Chen and Y. Huang, Enantioselective Seleno-Michael Addition Reactions Catalyzed by a Chiral Bifunctional N-Heterocyclic Carbene with Noncovalent Activation, *Angew. Chem., Int. Ed.*, 2022, **61**, e202202040.
- 69 C. Cui, Q. Li, Z. Wang, Y. Lu and X.-H. Yang, Catalyst-Controlled Divergent Cyclopropene Hydroselenation, *ACS Catal.*, 2025, **15**, 8855–8864.
- 70 A. Temperini, M. Ballarotto and C. Siciliano, Chemoselective and metal-free reduction of  $\alpha,\beta$ -unsaturated ketones by *in situ* produced benzeneselenol from O-(tert-butyl) Se-phenyl selenocarbonate, *RSC Adv.*, 2020, **10**, 33706–33717.
- 71 Y. Nishiyama, Y. Makino, S. Hamanaka, A. Ogawa and N. Sonoda, Selective reduction of  $\alpha,\beta$ -unsaturated carbonyl compounds with carbon monoxide and water assisted by selenium, *Bull. Chem. Soc. Jpn.*, 1989, **62**, 1682–1684.
- 72 H.-C. Li, C. An, G. Wu, G.-X. Li, X.-B. Huang, W.-X. Gao, J.-C. Ding, Y.-B. Zhou, M.-C. Liu and H.-Y. Wu, Transition-metal-free highly chemoselective and stereoselective reduction with Se/DMF/H<sub>2</sub>O system, *Org. Lett.*, 2018, **20**, 5573–5577.
- 73 Y. Nishiyama, M. Yoshida, S. Ohkawa and S. Hamanaka, New agents for the selective reduction of the carbon-carbon double bond of  $\alpha,\beta$ -unsaturated carbonyl compounds, *J. Org. Chem.*, 1991, **56**, 6720–6722.
- 74 M. J. Perkins, B. V. Smith and E. S. Turner, Photochemical reduction of carbon-carbon and carbon-nitrogen double bonds by benzeneselenol, *Chem. Commun.*, 1980, **20**, 977–978.
- 75 T. Masawaki, Y. Uchida, A. Ogawa, N. Kambe, N. Miyoshi and N. Sonoda, A novel oxygen induced reduction of  $\alpha,\beta$ -unsaturated carbonyl compounds by benzeneselenol, *J. Phys. Org. Chem.*, 1988, **1**, 115–117.
- 76 CCDC 2348172: Experimental Crystal Structure Determination, 2026, DOI: [10.5517/ccdc.csd.cc2jtghb](https://doi.org/10.5517/ccdc.csd.cc2jtghb).

